communications physics

Article

https://doi.org/10.1038/s42005-024-01619-4

Memory of elastic collisions drives high minority spin and oscillatory entropy in underdamped chiral spinners

Check for updates

Shengkai Li[1,2,8], Trung V. Phan[3,8], Gao Wang[4,5], Ramzi Khuri[6], Jared W. Wilson[1], Robert H. Austin[1] ✉ & Liyu Liu[7] ✉

Inertial underdamped collisions preserve the memory of physical parameters that existed before the collision, leading to phenomena usually unseen in overdamped systems. Here we probe the less studied inertial chiral matter with spinners on an air table. We show here the emergence of high levels of spin for a minority of (+) handed spinners in the presence of a majority of (−) handed spinners (vice versa). This deep violation of equipartition occurs due to the inertial (memory preserving) nature of elastic collisions between underdamped translating and rotating objects. Underdamped spinners of the same spin sign annihilate their spins when they elastically collide, transferring their spin angular momentum into orbital angular momentum, while oppositely handed spinners tend to preserve their individual spin levels, leading to the pumping of minority spinners to high spin levels. Entropy production and the flow of entropy in this underdamped system are also counter-intuitive, showing dramatic oscillations in time.

Underdamped active matter describes collections of driven objects that collide but do not immediately lose their individual momenta (both rotational and translational) before subsequent collisions. Underdamping of the vector momenta (inertia) results in the vector momenta being carried forward irreversibly in time to the next collision, a memory of what happened. Such time-irreversible motions give rise to quite complex, difficult to compute yet very important phenomena[1]. In the case of the Navier-Stokes equation the emergence of turbulence is due to the non-linear convection $(\vec{v}\cdot\nabla)\vec{v}$, very much an area of current active research[2]. In spite of their importance, typically in active matter work inertial effects are ignored because the scale of the motions studied can be at low Reynolds numbers where motions are time-reversible[3,4] and the difficulty of projecting forward in time subsequent collisions carrying memory of the past collisions. Because of the importance of inertia in many forms of active matter, time-irreversible active matter dynamics have gained attention[5]. Inertial memory effects have been found to induce phenomena unseen in overdamped systems, including enhancement of motility-induced phase separations[6,7], enhanced diffusion[8], and stochastic dynamics[9]. Many studies of inertial active matter have been concerned with linear inertial momenta dynamics, less attention has been paid to rotational (chiral) inertial underdamped aspects in elastic collisions[10]. Since even chiral active overdamped matter has been found to exhibit rich collective behavior[11–13], we explore here experimentally how inertial spin-orbital/angular momentum coupling can give rise to unexpected phenomena not seen in overdamped systems[14].

We consider the dynamics of a collection of translating and spinning objects (spinners) whose collisions are almost elastic and whose motion is highly underdamped, so that the kinetic results of the collisions are carried forward in time, hence subsequent motions have memory of previous motions. The relative spin handedness of the colliding spinners further alters the memory of their previous motions in unusual ways. More concretely, spin is a vector $\vec{S}$ defined as the localized angular momentum due to rotation of an object around its center of mass, $\vec{S}=\vec{\vec{I}}_{cm}\vec{\omega}$, where $\vec{\omega}$ is the spin vector of the object, and $\vec{\vec{I}}_{cm}$ is the moment of inertia tensor around the center of mass. Orbital angular momentum $\vec{L}_o$ is due to the rotation of the center of mass of an object with velocity $\vec{v}$ around some abstract fixed point a distance $\vec{r}$ from the center of mass of an object: $L_o = m\vec{r}\times\vec{v}$. In the case of inertial (elastic and underdamped) collisions, total angular

[1]Department of Physics, Princeton University, Princeton, NJ 08544, USA. [2]Center for the Physics of Biological Function, Princeton University, Princeton, NJ 08544, USA. [3]Yale University, New Haven, CT 06520, USA. [4]Wenzhou Institute, University of Chinese Academy of Sciences, Wenzhou, Zhejiang 325000, China. [5]School of Physical Sciences, University of Chinese Academy of Sciences, Beijing 100049, China. [6]Department of Natural Sciences, Baruch College, City University of New York, New York, NY 10010, USA. [7]Chongqing Key Laboratory of Soft Condensed Matter Physics and Smart Materials, College of Physics, Chongqing University, Chongqing 401331, China. [8]These authors contributed equally: Shengkai Li, Trung V. Phan. ✉e-mail: austin@princeton.edu; lyliu@cqu.edu.cn

momentum $\vec{L} = \vec{L}_o + \vec{S}$ is conserved but it is redistributed between the spin $\vec{S}$ and orbital angular momenta $\vec{L}_o$. When the motion of the spinners is underdamped, the final motion of two interacting spinners is strongly influenced by this redistribution of spin and orbital angular momentum. While collective behaviors of spinners have been extensively studied[1,15–18] and found with interesting phenomena such as odd elasticity[11,12] and odd viscosity[13], less attention has been paid to underdamped spinners than overdamped spinners. Perhaps the work closest to underdamped spinners is that of Workamp et al.[19] which does involve spinners that, while externally driven, are underdamped. To investigate the role of inertia in internally-driven spinners, here we introduce spinners with an explicit coupling between the spin and orbital angular momentum which drives fundamental processes such as spin pumping and entropy oscillations, not seen in[19].

In our case, each spinner generates its spin internally by on-board air blowers (see Supplementary Notes 1 and 2 for details), rather than be driven passively via high hydrodynamic drag of an external field, and thus the usual hydrodynamic approximations cannot be applied to our system. Further, we couple as strongly as possible spin-spin interactions during collisions using sharp teeth. Lastly, the flipping of spins in collisions is one of the aspects of our system that differs from previous work.

Our work is a mixture of experiment, theory, and simulation. There have been pioneering simulation studies of active spinners at very high densities[20], and pioneering experiments in biological collective dynamics which are overdamped have seen some of the phenomena we observe here[21,22], our experiments reveal phenomena neither predicted nor seen in these earlier studies.

Results

We achieved low damping by floating internally driven rotational discs (our spinners, 7 cm in diameter) on a rectangular air table (56 cm × 76 cm). The teeth of our spinners were offset from the taut wire of the boundary of the table, so that collisions of the spinners with the taught wire were highly elastic in terms of center of mass kinetic energy and did not change spin rates. Instead of using passive structures converting upward air into self rotation[23,24], here energy is fed into the system in two ways: (1) via incoherent drive via the turbulent air flow of the air table; (2) directly and locally by constant torque spin drive on each disc by opposing battery powered air blowers on each disc. The spin degrees of freedom are coupled to orbital degrees of freedom in collisions via teeth on the perimeters of the discs. Teeth-teeth interactions provide for strong coupling in collisions between spinners in a rather non-intuitive manner depending on the relative signs of the spin vectors of the colliding spinners. We call a counterclockwise (CCW) spinner having + spin, and a clockwise (CW) spinner having −spin.

Colliding spinners with the same sign of spin vector after a collision have tangential velocity vectors which are opposed in sign converting spin angular momentum into orbital angular momentum, annihilating their spins. This transfer of spin momentum into oppositely directed orbital angular momentum, since the outgoing velocities are at right angles to the incoming velocities this kind of energy transfer is somewhat analogous in semiconductors to the Hall effect. These momenta perpendicular to the flow of spinners resemble the electric charges trying to move perpendicular to the current in the classical Hall effect.

However, collisions between spinners of opposite sign tend to maintain their spin vectors since the tangential velocity vectors of the teeth are in the same direction and transfer little rotational energy into orbital angular momentum[13,25], exiting after a collision elastically with flipped input velocities and no change in spin. See Fig. 1 for a pictorial description of the process in the case of parallel spin vector collisions.

The above comments are for direct head-on collisions with zero impact parameters. We have derived the spin interchange averaged over all impact parameters b for a two-body spinner collision in Supplementary Note 3. When the initial angular velocities of the two colliding spinners are ω_1 and ω_2, the exiting angular velocities ω_1' and ω_2', respectively, are

$$\omega_1' - \omega_1 = \omega_2' - \omega_2 = -\beta(\omega_1 + \omega_2). \tag{1}$$

where R, M, *and* I are the radius, mass, and moment of inertia of an spinner. $\beta = 1/2(1 + I/MR^2) < 1/2$. Figure 2 shows experimental measurements of the rotational changes in collisions and the theoretical prediction. While there is noise in the data giving variances from the theory, the major take-away from this is that 1. the negative correlations in ++ and −− cases show annihilation of spin for same-sign collisions. 2. the smaller magnitude of + − interactions shows there is small or no change of spin for opposite-sign collisions. We will discuss these later in detail and show Eq. (1) leads to features of the collective motion.

Eq. (1) and the impact of spin-spin interactions for parallel spins has unexpected predictions which we exploited in the following 3 experiments.

Experiment 1: Spin Pumping of Minority Handedness

If both spinners have the same sign for the initial spin (a++ collision) they *lose* spin angular momentum which gets converted to orbital angular momentum, while spinners of the opposite sign (a+− collision) *maintain* spin angular momentum depending on the relative magnitudes of the angular velocities, with zero loss if $\omega_1 = -\omega_2$. Thus, a lone down (for example) spinner in a population of all up spinners on average maintains a greater spin (and spin kinetic energy) due to the less loss of spin in up-down collisions (see Fig. 3). This we call minority spin pumping.

The phenomenon of minority spin pumping is subtle. In addition to the simple case where spins have comparable magnitudes ($|\omega_1| \approx |\omega_2|$), in cases where one spin magnitude is much smaller than the other, Eq. (1) shows that the spinner with a larger spin will transfer its spin to the other one with a much smaller spin, but will flip the smaller spin sign. For instance, when spinner 1 having spin + Ω collides with spinner 2 having spin $\epsilon \ll \Omega$, spinner 1 transfers 3/8Ω to spinner 2, leaving itself with + 5/8Ω and flips spinner 2 to − 3/8Ω. Thus, spin re-distributions in sign are rather complex and non-intuitive, and highly dependent on the initial spin levels of the colliding spinners.

The phenomena of minority spin-pumping is experimentally seen in Fig. 4 (particularly Fig. 4b). Experiments were carried out as a function of the density of the spinners on the air table (Fig. 4a). At low spinner density most collisions are binary in nature and Eq. (1) can be used to predict the amount of transfer of spin angular momentum, which is constantly being pumped in by the tangentially configured blowers, into orbital angular momentum by collisions.

We applied both theory and simulation to understand these phenomena. Conservation of angular momentum is the fundamental physics of the collision as shown by Eq. (1), which is in good agreement with data of collisions extracted from experiments (see Fig. 4d). Based on this, we can create an inertia-dominated toy-model which allows us to write down the equation of rotational motion for each spinner.

$$\begin{aligned}\frac{d}{dt}\langle\omega_\pm\rangle \approx & \frac{N_\pm - 1}{N-1}\left[-\frac{\beta\left(\langle\omega_\pm\rangle + \langle\omega_\pm\rangle\right)}{\tau}\right] \\ & + \frac{N_\mp}{N-1}\left[-\frac{\beta\left(\langle\omega_\pm\rangle + \langle\omega_\mp\rangle\right)}{\tau}\right] \pm \frac{\int \Gamma_{\omega_\pm(t)}dt}{\tau}\Big|_{\langle\omega_\pm\rangle}\end{aligned} \tag{2}$$

Here, the first and second terms in Eq. (2) are the angular velocity decrease and change from same-spin and opposite-spin collisions. The third term is the angular velocity picked up between the collisions where $\pm\Gamma_{\omega_\pm} = \pm\gamma\left(1 \mp \frac{\omega_\pm}{\Omega}\right)$ is the external torque from the blowers and air drag. τ is the characteristic collision time. γ is the torque from the blower. $(\gamma/\Omega)\omega_\pm$ is the rotational air drag. The measurement of these constants can be found in Fig. S5 of the supplementary document.

After time-averaging many collisions for all spinners in each species, the steady-state solution to Eq. (2) leads to the estimation for the average

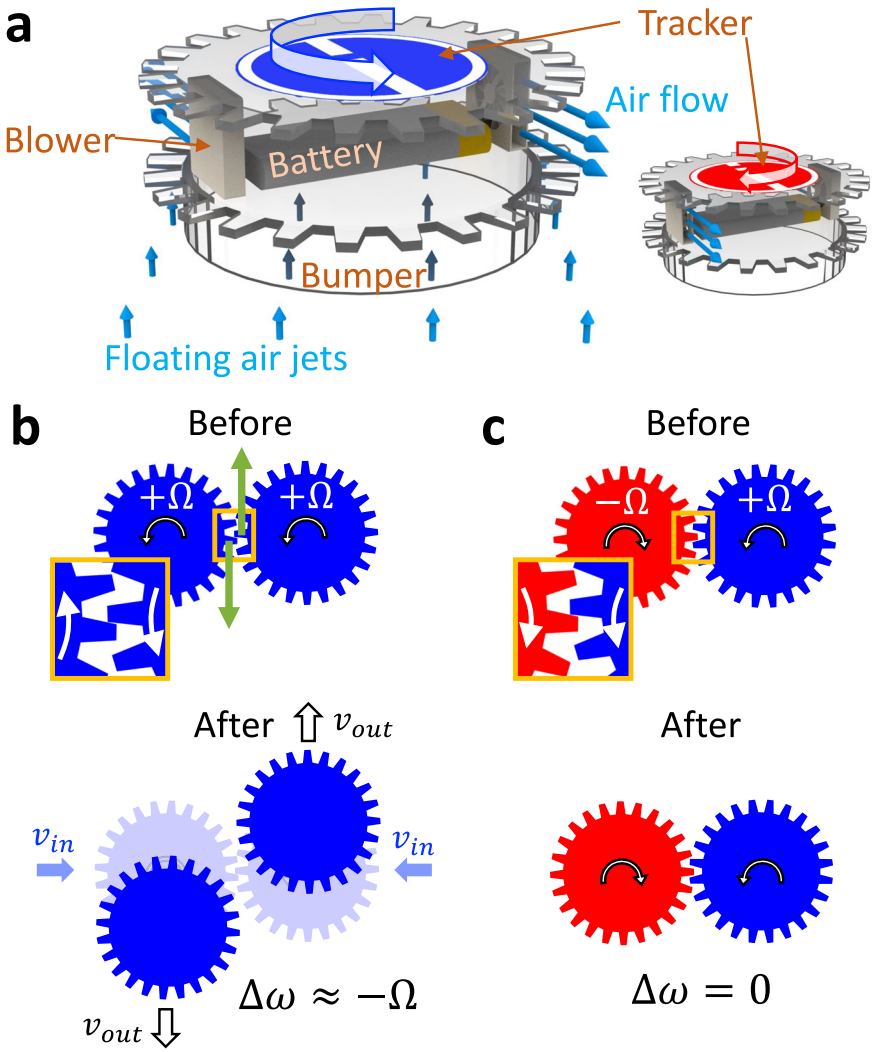

Fig. 1 | Basics of the spinners. a Air ejected from two blowers on the sides of the geared discs in opposite directions rotates a spinner (7 cm in diameter) floating on an air table. A tracker with a binary barcode mounted at the top of the spinner tracks its rotation and translation. Blue and red are used for CCW and CW spinners respectively. A bumper (a plastic dish) at the bottom elevates the spinner to avoid collision between the boundary wire and the blowers. **b** Two spinners with the same spins repel each other due to the opposite motion of gear teeth. From the collision, rotation is converted into oppositely directed translation motion with spin angular momentum converted into orbital angular momentum. **c** Two spinners with opposite spins have teeth motion in the same direction. See Supplementary Movie 1 for sample collisions.

spinning velocity $\langle\omega_\pm\rangle$ from the population number $N_\pm$:

$$\langle\omega_\pm\rangle = \pm\Omega\times\frac{\alpha(\alpha+3N-2-2N_\pm)}{(\alpha+2N-2)(\alpha+N-2)}, \tag{3}$$

where α depends on the inertial properties of the spinners and the driving torques generated by the air-blowers, and Ω is the maximum spin angular velocity the spinners can possibly be. For a fixed value of N then $\langle\omega_\pm\rangle$ monotonically decreases as $N_\pm$ increases: the minority will always spin faster than the majority. As shown in Fig. 4c, this model matches with experimental observations. Simulations using parameters measured from experiments also showed agreement with the results on energy and mixing dynamics' dependence on the spin ratio (Fig. S15). Our simulation shows that the concave geometry alone can generate the tangential interaction between spinners without using friction as a substitute in simulation[26]. As expected, after we remove all dissipative forces (orbital and rotational aerodynamic drag) and energy injection (rotational torque from the air blowers on the spinners), the orbital and rotational energies show equipartition in the simulation (see part B of the Supplementary Note 7 and Supplementary Movie 5).

Emergent spin currents are observed. The difference between collisions of the same- and opposite-handedness spinner pairs creates different emergent spin rate distributions and spatial currents depending on the ratio between the left-handed and right-handed spinners. The concave-down behavior of the total rotational energy centered at $n_+ = 1/2$ and the asymmetry of the orbital energies as functions of species populations (see Fig. 4) can be captured by crude estimations:

$$E_{all,rot} \propto \Omega^2\phi^{-2}\left[1-3\left(1/2-n_+\right)^2\right], \tag{4}$$

$$E_{\pm,orb} \propto \left[(3-2n_\pm)^2+\mathcal{E}\right]n_\pm \tag{5}$$

where $n_\pm = N_\pm/N = 1-n_\mp$, ϕ is the area fraction ($A_{spinners}/A_{arena}$), and $\mathcal{E}$ is the normalized variance of translational energy. See Supplementary Note 4 for details.

Figure 4 shows the rotational and orbital energy/spinner for $N = N_+ + N_- = 18$ spinners as a function of the n_+ in steady state. We stress several key points of these data. (1) Clearly at extrema/minima values of n_+ localization of the spin energy in the minority fraction is very clear; (2) At extrema/minima values of n_+ the high rotational energy of the minority spin substantially deducts rotational energy from the overall per spinner average rotational energy; (3) The average translational energy of the system per spinner is close to 1/10 the average rotational energy of the spinners, agreeing with the finding by Nguyen et al[27] at $\phi = 0.16$, the density of the experiment in Fig. 4; (4) At extrema/minima values of n_+ the spin-pumped spinners also extract translational energy from the spinners. Given the mirror symmetry, physical quantities including the kinetic energies should be symmetric about $n_+ = 1/2$ since an $n_+ = n_0$ experiment is a mirror image of an $n_- = n_0$ (i.e. $n_+ = 1-n_0$) experiment. While this symmetry is also

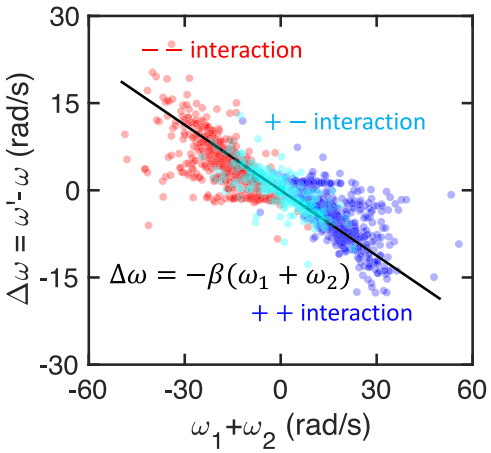

Fig. 2 | Collision rules. Change of angular velocity of both spinners is proportional to the sum of both velocities before collision (Eq. (1)). Here $\Delta\omega = \omega' - \omega$ uses the average of both spinners $\Delta\omega = (\Delta\omega_1 + \Delta\omega_2)/2$. The black theory line uses measured mechanical constant $\beta \sim 3/8$ measured (see Supplementary Note 3[46]). The color dots show the result from 10^4 collision events in experiments. The red, cyan, and blue dots show the $--$, $+-$, and $++$ collisions respectively.

confirmed in simulation (Fig. 4e, f), slight mechanical asymmetry due to the height difference of the battery between + spinner and − spinner (about 1 cm) leads to a small deviation from symmetry in experiments. Simulations further show the features above also hold for systems with large N. In an arena doubling both the width and length of the smaller one used in the experiment, spinners quadrupled in number retaining the same area fraction $\phi = 0.16$ show that the dependence of kinetic energies on the spin ratio remains very close to that of the smaller system. See Supplementary Note 7 and Fig. S16 of the supplementary document for details.

Experiment 2: Spatial Entropy Oscillation and Mixing Times

An interesting aspect of strong spin-spin interactions is the dependence of the spatial flow of mixing (positional) entropy on the net handedness of the mixture of spinners (Fig. 5). Since there is a directed (Hall) flow of energy from collisions of parallel spins to translational energy, there should be a strong dependence of spatial entropic mixing times on the net handedness of the spinner mixture, and a net generation of vorticity at interface boundaries between spin populations.

Note that all our spinners are identical (other than the sign of their torque drive) but distinguishable due to the code written on each one. Mixing entropy was computed by tracking individual spinners as to their position in the upper u and bottom b position over time, where we divided our spinners by their position in the upper u and bottom b region of the table starting at $t = t_0$. Instead of using a full description of microstates which would lead to the full entropy, here we use a partition of two subsystems to highlight the global characteristics. The positional entropy change S of an ensemble of spinners at a given time is then given by:

$$S(t_0 \to t) = -\left[p_u^u \ln p_u^u + p_u^b \ln p_u^b + p_b^b \ln p_b^b + p_b^u \ln p_b^u\right] \qquad (6)$$

where p_u^u is the probability of finding a spinner originally in the up location still in the up location at time t, p_u^b is the cross probability of finding a spinner originally in upper location now in the bottom location, etc. At $t = \infty$ for a uniform mixture $S(t_0 \to \infty) = S_{max} = 4 \times -[0.5 \ln(0.5)] = 2 \ln 2$, while at $t = t_0$, $S(t_0 \to t_0) = 0$ since all the cross probabilities are 0. In terms of microstates prescribed by $S_u^u \times S_u^b \times S_b^b \times S_b^u$ where the sets S correspond to the four types of spinners introduced above, among the states prescribed by the number of spinners in each set $\mathbf{N} = \{N_u^u, N_u^b, N_b^b, N_b^u\}$, state $\mathbf{N} = \{N/4, N/4, N/4, N/4\}$ has the most microstates and is the state the experiments gets to, either monotonically or oscillatorily.

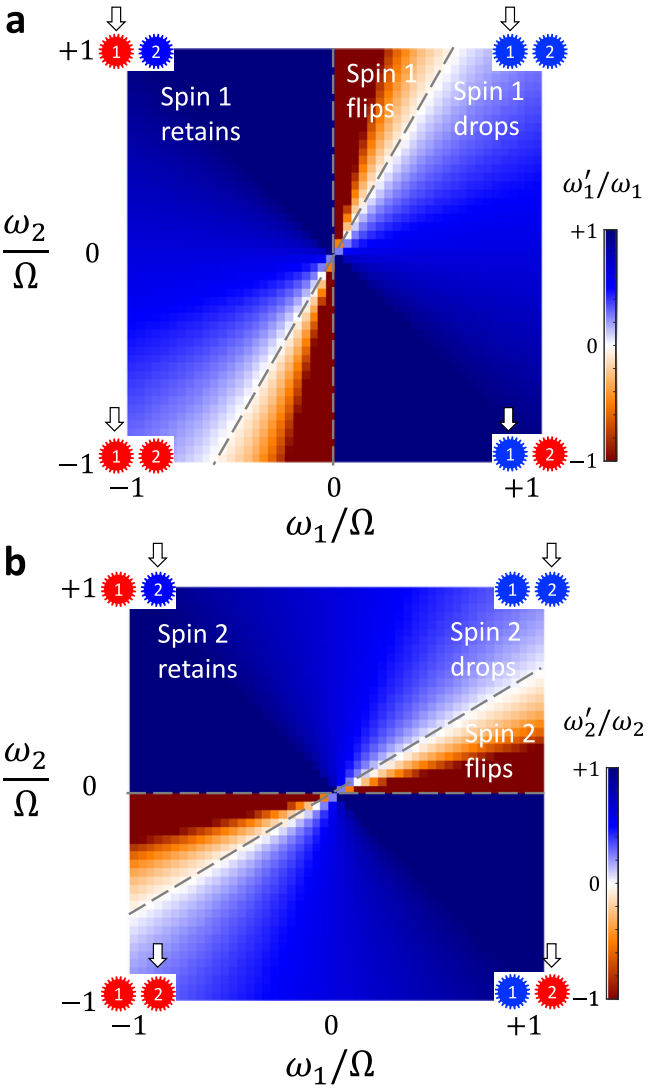

Fig. 3 | Spin flips for binary collisions. Panels **a** and **b** show the ratios between the spins after (ω_i') and before (ω_i) the collisions using Eq. (1) for the two spinners of concern, 1 and 2, respectively. They show that when $\omega_1 \approx \omega_2$ (around the diagonal), both spins drop significantly ($\omega_i'/\omega_i \ll 1$) after the collision and can be flipped (red region); when $\omega_1 \approx -\omega_2$, both spins mostly retain their spins ($\omega_i'/\omega_i \approx 1$) after the collision.

Entropy change $S(\tau)$ was measured by marking the spinners in the two sides of the arena (Fig. 5a, Supplementary Movie 3) and sampling over increasingly separated in time placements of the spinners:

$$S(\tau) = \langle S(t_i \to t_i + \tau)\rangle_i. \qquad (7)$$

We evaluated the difference between the entropy change $S(\tau)$ and its maximum S_{max} at a steady state after cutting the initial transient part when the air table gas jets are activated.

$S(\tau)$ generally increases with time as is expected for mixing (Fig. 5b). However, when the spinner density is high enough, we see oscillations in $S(\tau)$ with time indicating the emergence of vorticity during mixing. This emergence of vorticity is most dramatic when all the spinners are parallel to each other, resulting in the transfer of the net global spin to a global net orbital angular momentum so that a circulation of the spinners transiently exists. This edge current at the outer boundary (see Fig. 5d for the current) is also observed in other systems with rotating objects[28–30]. These oscillations do not appear for balanced initial spin states (Fig. 5e). For the 36-spinner experiments (area fraction $\phi = 0.32$), the spin ratio interval for no-oscillation

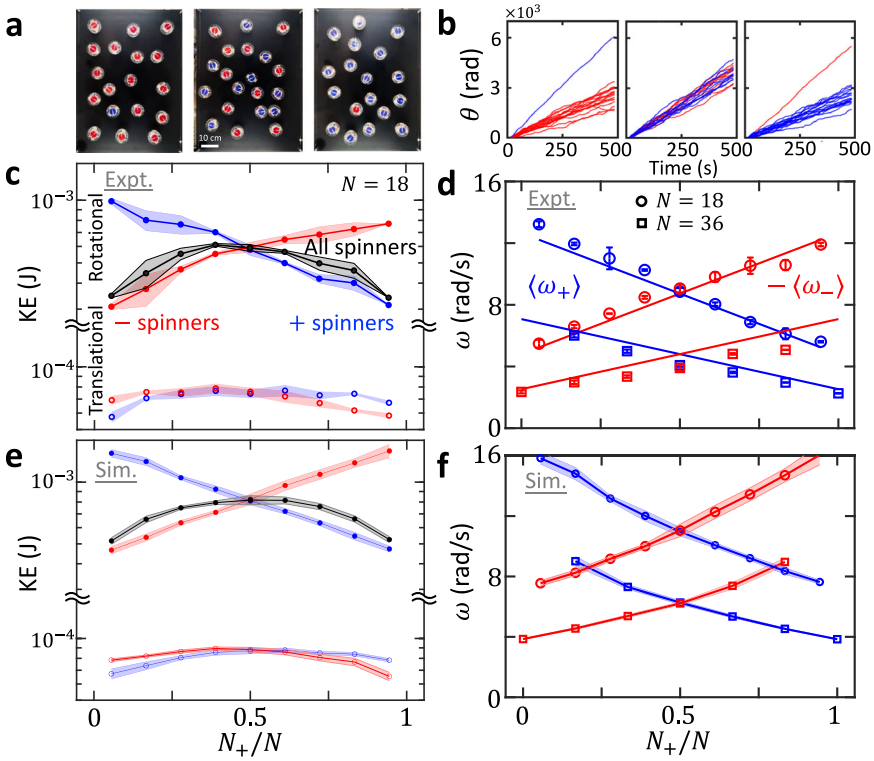

Fig. 4 | Effects from the spin-up/spin-down population ratio. a Three typical mixtures of the up and down spinners. **b** The evolution of self spin in spin-down dominant, even mixed, and spin-up dominant cases. The blue and red curves show the self-spin temporal evolution of all 18 spinners. See Supplementary Movie 2 for sample movies. **c** Orbital (open dots) and rotational energies (solid dots) per spinner averaged over time for various spin mixture ratios over 18 spinners. Blue and red curves show the energies of the spin-up (CCW, blue) and the spin-down (CW, red) respectively while the black curve shows the overall statistics. **d** Measured spin rate (error bars) compared with theory (Eq. (3), solid lines) using parameters $\Omega = 32$ rad/s and $\alpha = 6$ measured from individual spinners (see Supplementary Note 3). Panels **e** and **f** are the simulation counterparts of panels **c** and **d**. See Supplementary Movie 6 for videos.

is $|n_+ - 1/2| < \Delta \approx 1/4$ (Fig. 5f). For the 18-spinner experiments (area fraction $\phi = 0.16$), Δ is almost 1/2. We show how the oscillation of the mixing entropy can emerge in Supplementary Note 5 and that the oscillation's dependence on area fraction ϕ and spin ratio $n_+ = N_+/N$ retains for larger N in Supplementary Note 7 and Fig. S17.

Another result is that the characteristic mixing time T_{mix} for the entropy change to relax to the maximum value peaks at even spin mixtures and is lowest when the spinners only have one species (Fig. 5c inset). This implies that initial even mixed spin states evolve more slowly presumably because little spin energy is transferred into translational orbital energy for anti-parallel collisions. Further, as the spin ratio n_+ approaches the region where the increase of mixing entropy does not oscillate, the number of vortices increases substantially from 1 (one unique global circulation) while the overall vorticity remains neutral since the positive vortices pair with the negative vortices[23]. The positions of the vortices move over time and vary over different experiments. These features are also observed in simulations (Fig. S5). Once the spin ratio n_+ is within the critical ratio, the vortices are much more local and motile, presumably slowing down the mixing process. We posit a two-species generalization of the field theory of spinners[26,28,31] could further explore the criticality of the spin ratio, and whether the non-monotonic increase of entropy persists for thermodynamic limit. The entropy oscillation reveals that in this system time-dependent mixing kinetics is like an "annealing" process for the entire system, which optimizes the spatial configurations of the spinners inside.

Experiment 3: Spin frustration

The influence of topology and spinner placement is informative. In a simple example of how topology and edge state placement greatly change the spinner dynamics, we placed 4 spinners within a floating circle of inner diameter D equal to 6 spinner radii, such that while the spinners could rotate under the applied blower torque and translate enough to freely collide, they could not exchange center of mass positions (see Fig. 6a). Under those conditions there are only two possible topologies for a zero net spin collective: 2 spinners side by side of like spin, or diagonally opposed.

The spinner dynamics became quite different because in the side-by-side topology++ spin annihilating collisions are allowed and thus spin kinetic energy is transferred to orbital kinetic energy, while in the diagonally opposed configuration only + − spin collisions are allowed, and thus high spin angular momenta should occur since the loss of spin kinetic energy is minimized. Figure 6c shows this to be the case: the parallel topology on average has low spin kinetic energy with a power-law-like probability distribution function, while the diagonal topology has a steady state of high spin kinetic energy with a peaked probability distribution function.

The floating confining ring can act as a transmission connecting spin dynamics within the ring to external rings so that in principle our spinner can become a scale-free fractal hierarchical structure by connecting to every increasing sized toothed rings. As a first-step demonstration of this, in Fig. 6b we observe that the floating ring dynamics are strongly determined by the topology of the spinners contained within the ring. The intermittency of observed rotational energies (Fig. 6d) indicates that this geometrically confined system of spinners is in frustration[32–34], as there exists no steady state. As the ring is slightly slacker than what will make all the spinners frustrated at the same time, only two or three spinners out of the four frustrate each other at the same time, leaving the other one or two charging up the spin and rotating the external ring for a short interval of time. This small but systematic net effect leads to intermittent bursts of the ring rotation and consequently the net rotation. We study other possible arrangements of 4 spinners in Supplementary Note 6, and also give an example of a scale-free fractal gear design there. Future studies would include designs of fractal gears in more levels, which would bring more complex and interesting spatial-temporal dynamics.

Conclusion

Our findings show how energy and entropy flow through the spin and orbital degrees of freedom via spin-dependent interactions when a system has memory. We discovered a spin-pumping mechanism that focuses spin kinetic energy on the spinner species with the smaller population number. Further, we observed the emergence of vorticity in the mixing entropy.

The inertial spinner swarm introduced here exhibits phenomena beyond conventional statistical mechanics[27,35,36] and poses many unsolved puzzles in number theory and classical mathematics[37,38]. In regards to fractal spinner[39], these chiral agents could provide a "gearbox"[40,41] whose mode

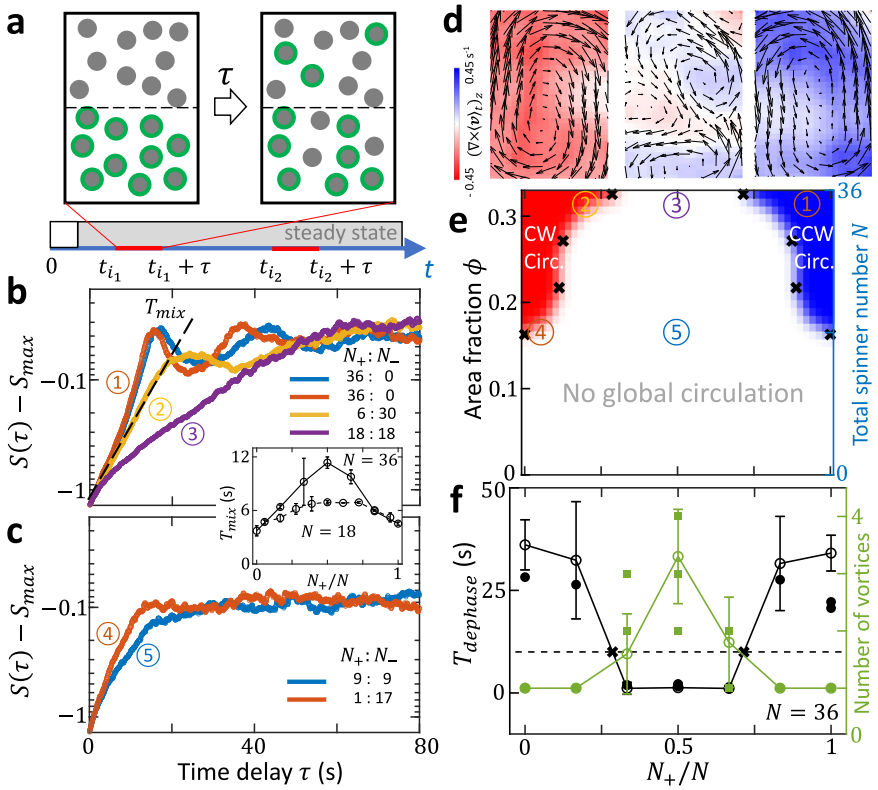

Fig. 5 | Entropy change. a To evaluate the entropy change in time τ, we mark spinners on both sides (lower part in green circles as an example here) at the beginning of a time interval and evaluate the entropy change after τ. One can find many such evolutions with time interval τ. We average the ensemble of these intervals for the entropy change $S(\tau)$. See Supplementary Movie 3 for visualization. **b** Entropy change approaches maximum over time for 36 spinners. The blue, orange, yellow, and purple curves show the results for two repetitions of N_+: N_- = 36: 0, one example of N_+: N_- = 6:30 and 18:18, respectively. The decay time for the incipient drop is used as the characteristic time for mixing (T_{mix}). **c**. Entropy changes over time for 18 spinners. The blue and orange curves show one example of N_+: N_- = 9: 9 and 1:17, respectively. Inset: Mixing time dependence on the spin ratio for both densities. **d** Time-averaged velocity of spinners for pure-bottom-spin, even, and pure-upper-spin collectives for 36-spinner collectives over 500 seconds. **e** Three distinct phases of the spinner collectives depending on the spin ratio and area fraction. The boundary of phases is determined by the sharp transition of dephasing time from simulation. **f** The black and green curves show the dephasing time ($T_{dephase}$, the characteristic time for the oscillation part of entropy increase to decay) and the number of emergent vortices at different spin ratios for 36-spinner collectives. The error bars and solid dots show the simulation and experiment, respectively. The phase boundary in **e** uses $T_{dephase}$ = 10 s as shown by crosses.

could be switched with a programmable[36] configuration of spins (Fig. 6b). Since each of the spinners is individually driven by battery-driven blowers, installation of active computational and sensor technology in each spinner will allow for the emergence of a fully interactive swarm of agents with memories of the past and physics predictions of the future[42,43].

Methods

Experiment setup

The spinners consist of toothed acrylic discs which are laser-cut to have 24 teeth. The spinners were driven by two oppositely directed blowers (SUNON UB3-500B), driven at 3.7 volts by a LiIon 400 mA-hr battery (Adafruit 3898). The battery was sandwiched between two of the toothed discs, so that change in handedness of the spin could be accomplished by an inversion of the disc. A 60mm-diameter plastic Petri dish (Falcon Plastics) was used to lift the toothed wheel so that the close-to-elastic collisions with the taut wire of the air table did not involve the teeth. Each spinner has a mass of 0.025 kg, and a moment of inertia about the center of mass of 1.02×10^{-5} kg m^2. See Supplementary Note 2 for measurement details.

The air table that floats the spinners is an Ealing Precision Air Table made by Boreal Science. It had honeycomb cores providing excellent strength and stability and a surface flatness of ± .025 cm. A steel wire bumper on the circumference kept the spinners bouncing off from the arena's boundary. Leveling screws on the three feet beneath the air table were used to adjust the levelness of the table.

An iPhone camera running at 30 frames/sec was used to take continuous movies of the dynamics of the spinner active matter. A bar code imprinted on the top of each spinner allowed us to keep track of the center of mass positions of individual spinners versus time, measure rotation of the bar code about the center of mass, and measure the spin angular momentum of each spinner as a function of time. To ensure the consistency of the rotational driving torque, we made sure the batteries did not run more than 30 minutes after being charged to full capacity.

Simulation

In the simulations, each spinner was subjected to a collision force and torque from another spinner $\mathbf{F}_{coll}, \tau_{coll}$, translational drag force $\mathbf{F}_{drag}^{trans}=-\eta\mathbf{v}=-\eta\dot{\mathbf{r}}$, rotational driving torque $\tau_{drive}=s_j\tau_{drive}^0$ from the blowers on spinner where $s_j=1$ for + spinners and $s_j=-1$ for − spinners, rotational drag torque $\tau_{drag}^{rot}=-\eta_\varphi\dot{\varphi}$, air current flow $\mathbf{F}_{air}$, and collision force from the boundary $\mathbf{F}_{wall}$. The parameters were determined from direct and indirect physical measurement as listed in Table 1.

For the spinner-spinner collision force, each spinner was modeled as line segments connected one to another. It used the exact geometry of the physical spinners. The spinner-spinner interaction was evaluated as the sum of all pairwise interactions between the line segments of the two spinners. In this work, each spinner had 24 teeth and $24\times4=96$ line segments. Therefore, there were 96^2 pairs of line-line interactions to sum up for two spinners. The line-line interaction used the spring-dash model, which regarded the strain as the virtual overlap of the two line segments

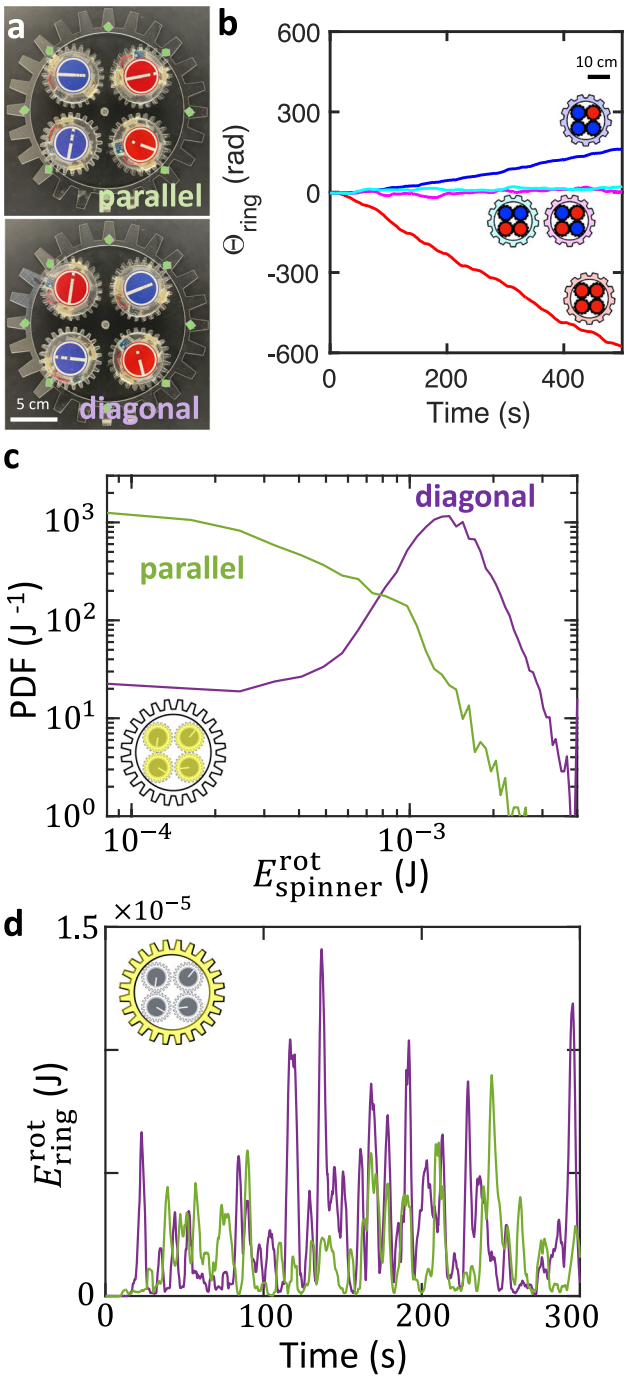

Fig. 6 | Confined spinners. a Two topologies: parallel and diagonal (Supplementary Movie 4). **b** Self spin Θ_{ring} of the ring depending on the configuration of spins inside. The blue, cyan, magenta, and red curves show the results for configurations N_+:N_- = 3:1, 2:2 (parallel), 2:2 (diagonal), and 0:4, respectively. **c** Probability distribution of rotational energies for the two topological edge configurations (green: parallel, purple: diagonal). **d** Transfer of spin energy to the outer floating ring for the two topologies (green: parallel, purple: diagonal).

$\mathbf{F}_{coll} = (k_s\delta + k_d\delta v_n)\hat{\mathbf{n}}$, where v_n was the relative velocity projected in the normal direction $\hat{\mathbf{n}}$ and δ was the deformation of the spinner segments. k_s and k_d were phenomenological parameters such that the coefficient of restitution and the collision pattern $\Delta\omega = -\beta(\omega_1 + \omega_2)$ matches with the experiment. In the simulation, we used $k_s = 10^4$ N/m, $k_d = 2 \times 10^5$ N s/m^2. For the collision force exerted by the wall, we neglected the damping such that $\mathbf{F}_{wall} = k_s\delta\,\hat{\mathbf{n}}$ where $\hat{\mathbf{n}}$ points inward the arena. In summary, the dynamic equations for integration read

$$m\ddot{\mathbf{r}}_j = -\eta\dot{\mathbf{r}}_j + \mathbf{F}_{coll,j} + \mathbf{F}_{air,j} + \mathbf{F}_{wall,j} \tag{8}$$

$$I\ddot{\varphi}_j = s_j\tau_{drive} - \eta_\varphi\dot{\varphi}_j + \tau_{coll,j}. \tag{9}$$

The simulation code was first developed in MATLAB for visual convenience and then manually compiled into C++ for efficiency. The numerical scheme used an symplectic integrator, the velocity-Verlet method[44] to reduce accumulated numerical errors. The time step used 10^{-4} second considering the largest Jacobian related to the collision was ~10^4 second^{-1} as we chose the collision elasticity to be 10^4 N/m. The elasticity was phenomenological and yet physically realistic such that the collision result was insensitive to the elasticity value, given the order of magnitude is ~10^4 N/m.

As a test, we evaluated a simulation at equilibrium conditions (without air current force, rotational or translation drag or drive) where 18 non-active spinners started with pure translational motion. Over time, a portion of translational energy gradually converted to rotational (spin) energy and eventually showed equipartition in rotational (1 degree of freedom) and translational energy (2 degrees of freedom), i.e. $\frac{1}{2}m\langle v_i^2\rangle_i/2 = \frac{1}{2}I\langle\omega_i^2\rangle_i/1$[45]. It is an interesting feature that with concave geometry, there can be a tangential interaction without dissipative forces[26].

For more details of the simulation, see Supplementary Note 7.

Table 1 | List of parameters used in simulations

	Description	Value	Reference
m	Spinner mass	0.025 kg	Direct measurement from a scale.
R_0	Spinner outer radius	0.035 m	Direct measurement from a caliper.
R_i	Spinner inner radius	0.030 m	Same as above.
I	Spinner moment of inertia	1.01×10^{-5} kg m^2	Supplementary Note 2.
Ω	Saturated angular velocity	32 rad s^{-1}	Fig. S5 in the supplementary document.
γ	Rotational driving acceleration	3.4 rad s^{-2}	Same as above.
τ^0_{drive}	Rotational driving torque	3.4×10^{-5} N m	$= I\gamma$.
η	Translational drag coefficient	1.6×10^{-3} kg s^{-1}	$= m \cdot 6.5 \times 10^{-2}$ s^{-1}. See Fig. S2D in the supplementary document.
η_φ	Rotational drag coefficient	1.06×10^{-6} N m s	$= \tau_{drive}/\Omega$.
F_{air}	Air current force		See the cubic fit in the inset Fig. S13A in the supplementary document.
A_1	Half arena length	0.38 m	Direct measurement from a meter stick.
A_2	Half arena width	0.28 m	Same as above.

Data availability

Supplementary movies 1 to 6 are available. Experiment data are available at zenodo.org/records/10899899.

Code availability

Code to evaluate the experiment data is available at zenodo.org/records/10899899.

Received: 18 August 2023; Accepted: 4 April 2024;
Published online: 27 April 2024

References

1. Te Vrugt, M., Frohoff-Hülsmann, T., Heifetz, E., Thiele, U. & Wittkowski, R. From a microscopic inertial active matter model to the schrödinger equation. *Nat. Commun.* **14**, 1302 (2023).

2. Nguyen, V. & Park, W. G. A review of preconditioning and artificial compressibility dual-time navier-stokes solvers for multiphase flows. *Fluids* **8**, 100 (2023).
3. Purcell, E. M. Life at low Reynolds number. *Am. J. Phys.* **45**, 3–11 (1977).
4. Marchetti, M. C. et al. Hydrodynamics of soft active matter. *Rev. Mod. Phys.* **85**, 1143 (2013).
5. Scholz, C., Jahanshahi, S., Ldov, A. & Löwen, H. Inertial delay of self-propelled particles. *Nat. Commun.* **9**, 5156 (2018).
6. Caprini, L., Gupta, R. K. & Löwen, H. Role of rotational inertia for collective phenomena in active matter. *Phys. Chem. Chem. Phys.* **24**, 24910–24916 (2022).
7. Dai, C., Bruss, I. R. & Glotzer, S. C. Phase separation and state oscillation of active inertial particles. *Soft Matter* **16**, 2847–2853 (2020).
8. Sandoval, M. Pressure and diffusion of active matter with inertia. *Phys. Rev. E* **101**, 012606 (2020).
9. Te Vrugt, M., Jeggle, J. & Wittkowski, R. Jerky active matter: a phase field crystal model with translational and orientational memory. *N. J. Phys.* **23**, 063023 (2021).
10. Löwen, H. Inertial effects of self-propelled particles: From active brownian to active langevin motion. *J. Chem. Phys.* **152**, 040901 (2020).
11. Scheibner, C. et al. Odd elasticity. *Nat. Phys.* **16**, 475–480 (2020).
12. Tan, T. H. et al. Odd dynamics of living chiral crystals. *Nature* **607**, 287–293 (2022).
13. Banerjee, D., Souslov, A., Abanov, A. G. & Vitelli, V. Odd viscosity in chiral active fluids. *Nat. Commun.* **8**, 1573 (2017).
14. Loewe, B., Souslov, A. & Goldbart, P. M. Flocking from a quantum analogy: spin-orbit coupling in an active fluid. *New J. Phys.* **20**, 013020 (2018).
15. Nguyen, G. H. P., Wittmann, R. & Lowen, H. Active Ornstein-Uhlenbeck model for self-propelled particles with inertia. *J. Phys.-Condens. Matter* **34**, 035101 (2022).
16. Caprini, L., Gupta, R. K. & Lowen, H. Role of rotational inertia for collective phenomena in active matter. *Phys. Chem. Chem. Phys.* **24**, 24910–24916 (2022).
17. Leoni, M. et al. Surfing and crawling macroscopic active particles under strong confinement: Inertial dynamics. *Phys. Rev. Res.* **2** (2020).
18. Barotta, J.-W., Thomson, S. J., Alventosa, L. F., Lewis, M. & Harris, D. M. Bidirectional wave-propelled capillary spinners. *Commun. Phys.* **6**, 87 (2023).
19. Workamp, M., Ramirez, G., Daniels, K. E. & Dijksman, J. A. Symmetry-reversals in chiral active matter. *Soft Matter* **14**, 5572–5580 (2018).
20. van Zuiden, B. C., Paulose, J., Irvine, W. T. M., Bartolo, D. & Vitelli, V. Spatiotemporal order and emergent edge currents in active spinner materials. *Proc. Natl Acad. Sci. USA* **113**, 12919–12924 (2016).
21. Drescher, K. et al. Dancing volvox: Hydrodynamic bound states of swimming algae. *Phys. Rev. Lett.* **102**, 168101 (2009).
22. Petroff, A. P., Wu, X.-L. & Libchaber, A. Fast-moving bacteria self-organize into active two-dimensional crystals of rotating cells. *Phys. Rev. Lett.* **114**, 158102 (2015).
23. López-Castaño, M. A., Seco, A. M., Seco, A. M., Rodríguez-Rivas, Á. & Reyes, F. V. Chirality transitions in a system of active flat spinners. *Phys. Rev. Res.* **4**, 033230 (2022).
24. Farhadi, S. et al. Dynamics and thermodynamics of air-driven active spinners. *Soft matter* **14**, 5588–5594 (2018).
25. Scholz, C., Engel, M. & Pöschel, T. Rotating robots move collectively and self-organize. *Nat. Commun.* **9**, 931 (2018).
26. Liu, P. et al. Oscillating collective motion of active rotors in confinement. *Proc. Natl Acad. Sci.* **117**, 11901–11907 (2020).
27. Nguyen, N. H., Klotsa, D., Engel, M. & Glotzer, S. C. Emergent collective phenomena in a mixture of hard shapes through active rotation. *Phys. Rev. Lett.* **112**, 075701 (2014).
28. Yang, X., Ren, C., Cheng, K. & Zhang, H. Robust boundary flow in chiral active fluid. *Phys. Rev. E* **101**, 022603 (2020).
29. Petroff, A. P., Whittington, C. & Kudrolli, A. Density-mediated spin correlations drive edge-to-bulk flow transition in active chiral matter. *Phys. Rev. E* **108**, 014609 (2023).
30. Yang, Q. et al. Topologically protected transport of cargo in a chiral active fluid aided by odd-viscosity-enhanced depletion interactions. *Phys. Rev. Lett.* **126**, 198001 (2021).
31. Tsai, J.-C., Ye, F., Rodriguez, J., Gollub, J. P. & Lubensky, T. A chiral granular gas. *Phys. Rev. Lett.* **94**, 214301 (2005).
32. Ramirez, A. Geometric frustration: Magic moments. *Nature* **421**, 483–483 (2003).
33. Ramirez, A. Geometrical frustration. *Handb. Magn. Mater.* **13**, 423–520 (2001).
34. Snyder, J., Slusky, J., Cava, R. & Schiffer, P. How 'spin ice'freezes. *Nature* **413**, 48–51 (2001).
35. Aref, H., Newton, P. K., Stremler, M. A., Tokieda, T. & Vainchtein, D. L. Vortex crystals. *Adv. Appl. Mech.* **39**, 2–81 (2003).
36. Li, S. et al. Programming active cohesive granular matter with mechanically induced phase changes. *Sci. Adv.* **7**, eabe8494 (2021).
37. Aref, H. & Vainchtein, D. L. Point vortices exhibit asymmetric equilibria. *Nature* **392**, 769–770 (1998).
38. Aref, H. Point vortex dynamics: a classical mathematics playground. *J. Math. Phys.* **48**, 065401 (2007).
39. Kriegman, S. et al. Scale invariant robot behavior with fractals. *Proceedings of Robotics: Science and Systems* **17**, 59 (2021).
40. Savoie, W. et al. A robot made of robots: Emergent transport and control of a smarticle ensemble. *Sci. Robot.* **4**, eaax4316 (2019).
41. Boudet, J.-F. et al. From collections of independent, mindless robots to flexible, mobile, and directional superstructures. *Sci. Robot.* **6**, eabd0272 (2021).
42. Wang, G. et al. Emergent field-driven robot swarm states. *Phys. Rev. Lett.* **126**, 108002 (2021).
43. Wang, G. et al. Robots as models of evolving systems. *Proc. Natl Acad. Sci.* **119**, e2120019119 (2022).
44. Swope, W. C., Andersen, H. C., Berens, P. H. & Wilson, K. R. A computer simulation method for the calculation of equilibrium constants for the formation of physical clusters of molecules: Application to small water clusters. *J. Chem. Phys.* **76**, 637–649 (1982).
45. Nichol, K. & Daniels, K. E. Equipartition of rotational and translational energy in a dense granular gas. *Phys. Rev. Lett.* **108**, 018001 (2012).
46. Schedlinski, C. & Link, M. A survey of current inertia parameter identification methods. *Mech. Syst. Signal Process.* **15**, 189–211 (2001).

Acknowledgements

This work was supported by the National Natural Science Foundation of China (11974066 and 12174041) and the US National Science Foundation (PHY-1659940 and PHY-1734030). We acknowledge useful discussions with Truong H. Cai, Huy D. Tran, Khang V. Ngo, Junang Li, and Endao Han.

Author contributions

S.L., T.V.P., R.H.A., and L.L. designed the research; S.L. performed the experiments; S.L., T.V.P., J.W.W., R.K., and R.H.A. analyzed the data; T.V.P. constructed the theoretical model; S.L. did the simulation; S.L., T.V.P., G.W., and R.H.A. discussed the results and prepared the figures; all authors wrote the paper.

Competing interests

The authors declare no competing interests.

Additional information

Supplementary information The online version contains supplementary material available at https://doi.org/10.1038/s42005-024-01619-4.

Correspondence and requests for materials should be addressed to Robert H. Austin or Liyu Liu.

Peer review information *Communications Physics* thanks the anonymous reviewers for their contribution to the peer review of this work. A peer review file is available.